Improved predictions of thermal fluid pressurization in hydro-thermal models based on consistent incorporation of thermo-mechanical effects in anisotropic porous media

J. Buchwald[a,b,*], S. Kaiser[b], O. Kolditz[a,c,d], T. Nagel[b,d]

[a] Helmholtz Centre for Environmental Research – UFZ, Permoserstraße 15, 04318 Leipzig, Germany
[b] Chair of Soil Mechanics and Foundation Engineering, Geotechnical Institute, Technische Universität Bergakademie Freiberg, Germany
[c] Applied Environmental Systems Analysis, Technische Universität Dresden, Germany
[d] TUBAF-UFZ Center for Environmental Geosciences

Abstract

Coupled thermo-hydro-mechanical models are commonly used to model the evolution of temperature, pore pressure, and stress in a wide range of geotechnologies such as geothermal applications or around canisters of high-level radioactive waste in deep underground storage facilities. Their numerical modelling is often computationally highly demanding, especially if parameter identification, sensitivity analyses or uncertainty quantification require many model evaluations. Often, the thermally driven pore pressure evolution and the subsequently altered flow processes are the primary targets of an analysis. To benefit from the computational efficiency of hydro-thermal (HT) models while maintaining the accuracy of thermo-hydro-mechanical (THM) model, we derived two cases of a simplified representation of mechanical deformations in a coupled hydro-thermal model. Deformations induced by pressure as well as temperature changes are consistently incorporated into the mass balance storage terms. We demonstrate the exact coincidence of THM and modified TH formulations in isotropic and orthotropic materials as long as the basic assumptions like constant hydrostatic stress conditions or uniaxial strain hold. By modeling of a point heat source in isotropic or anisotropic porous media it is shown that a good agreement between TH and THM models can be maintained even though the assumptions underlying the simplification are no longer valid exactly. On our test-machine, a significant speed-up could be achieved by the reduction of the problem size when transitioning from a THM to a TH model. The highest speed-ups were achieved when Taylor-Hood elements were employed in order to avoid the problem of spurious pressure oscillations in the fully coupled THM model.

Keywords: thermo-hydro-mechanical, hydro-thermal, radioactive waste, geological repository,

specific storage, model complexity reduction, OpenGeoSys

2000 MSC: 74-10, 74F05, 74F10, 74E10

1. Introduction

The scope of coupled thermo-hydro-mechanical (THM) models ranges from studying natural phenomena to applications in geotechnical and civil engineering, materials processing and the chemical industry. Recent applications of THM analyses include supercritical geothermal systems in hot regions of the earth's crust [1] and, in general, the engineering of geothermal systems [2, 3, 4, 5, 6]. Both porous and fractured media are of interest in geoscientific applications: for example, fault discontinuities in aquifers [7] or seismic faults [8] are studied using THM models as well as various problems in the field of hydraulic fracturing [9, 10, 11]. Enhanced oil and gas recovery [12, 13] or CO_2 sequestration are other prominent fields of application for THM models [14, 15].

Viewing this diversity from another perspective highlights the variety of materials that is investigated with THM models; among them are concrete [16], soils [17, 18, 19], gas-hydrate-bearing sediments [20], granite [21, 22], sandstone [23], limestone [24], silt [25], smectite [26], clay [27], or even municipal solid waste [28, 29, 30, 31]. Nuclear waste disposal research often investigates the behaviour of clay rocks [32, 33, 34, 35], bentonite [36, 37, 38] or their combination [39] using THM models. Other authors investigated tuff [40], rock salt [41], or granite [42].

Although widely used, THM modeling of many geotechnical problems remains a costly task and often requires a number of simplifications to remain feasible with the available resources. Computational costs becomes specifically relevant when dealing with multiscale phenomena [43] or when a high number of model evaluations is needed (e.g., for uncertainty quantification). One of the main drivers of computational cost is the consideration of deformation processes. Even if mere elasticity is considered, numerical stability requirements can lead to a rapid increase in the degrees of freedom of the discretized system compared to thermo-hydraulic (TH) or hydro-thermal analyses which neglect mechanics altogether. The latter are therefore common alternatives to fully-coupled THM analyses if flow is the main concern instead of rock mechanics. Such TH models, however,

*Corresponding author

tend to overestimate pore pressure evolution due to the assumption of a rigid pore space. This may be alleviated by considering hydraulic storage effects, but their parameterization in the presence of thermal effects and anisotropy remains unclear.

There exist some theoretical works that adjusted a non-trivial storage term, namely [44] and [45], who derived expressions under constant stress and uniaxial strain conditions for the application of hydraulic flow in aquifers or very recently [46], who used an adapted TH model to describe the pore pressure response of radioactive waste in Callovo-Oxfordian claystone. These expressions have been successfully applied by others [47, 48, 49, 50], for example to derive storage coefficients for different porosity models in coal and under uniaxial strain conditions. What is needed is an explicit expression of compressibility and thermal expansion terms as they appear in coupled TH and in THM models as part of the mass and momentum balance equations [51, 52, 53].

To our knowledge, however, no theoretical works presented storage coefficients for TH models consistently derived from THM models considering both isotropic and anisotropic elasticity. In our manuscript, we thus investigate and compare two limiting cases of the implicit consideration of mechanics in models of non-isothermal flow through porous media composed of compressible phases: one that is based on the assumption of constant hydrostatic stress and another that is based on uniaxial strain under a constant normal stress.

The article commences by verifying exact correspondence of both implementations as long as the simplifying assumptions are honored. We then compare modeling results of thermal pressurization around a point heat source embedded in an orthotropic elastic medium to demonstrate the relevance of both implementations for applications such as high-level radioactive waste canisters embedded in saturated argillaceous formations. Finally, to illustrate the method's use in a more realistic setting with heterogeneous material properties, a cylindrical heat source surrounded by three different media types is considered. Significant reductions of computing times were achieved while the pore pressure predictions remained close to those of the fully-coupled THM model.

2. The underlying multiphysical THM problem

As a starting point for our derivation, we select a coupled thermo-hydro-mechanical (THM) model of a fluid-saturated porous medium. The model can be formulated in terms of the three primary variables temperature, pore pressure, and displacement in the balance equations of mass, momentum, and energy, complemented by the constitutive relationships of the fluid and solid phases and their interaction in the context of porous-media mechanics [54, 55]. Analytical solutions exist only for a hand-full of cases of high symmetry [56, 57, 58, 59].

To understand the model, consider the case of a heat source embedded in such a fluid-saturated porous medium. The essential physical processes can be described as follows: The heat source induces an increase in local temperature, causing both, solid and fluid to expand. The differential expansion of the phases creates pore pressure and effective stress variations. The resulting pressure gradient causes the fluid to flow away from the heat source, resulting in a dissipation of the pore pressure in a thermally driven consolidation process. The corresponding equations of the linear problem can be written in terms of energy, mass and linear momentum balance equations that are coupled to each other via primary variables and constitutive relationships. The thermal part is described in terms of the energy balance equation which reads (for a brief nomenclature, see Tab. 2)[1]

$$(\rho c_p)^{\mathrm{eff}}\dot{T} + \rho_{\mathrm{L}} c_p^{\mathrm{L}} T_{,i} (w_{\mathrm{L}})_i - \left(\lambda_T^{\mathrm{eff}} T_{,i}\right)_{,i} = Q_T \ , \tag{1}$$

where Q_T is a heat source per unit volume and the macroscopic effective parameters are given by

$$(\rho c_p)^{\mathrm{eff}} = \phi_{\mathrm{F}} \rho_{\mathrm{L}} c_p^{\mathrm{L}} + (1 - \phi_{\mathrm{F}})\, \rho_{\mathrm{S}} c_p^{\mathrm{S}} \ , \tag{2}$$

$$\lambda_T^{\mathrm{eff}} = \phi_{\mathrm{F}} \lambda_T^{\mathrm{L}} + (1 - \phi_{\mathrm{F}})\, \lambda_T^{\mathrm{S}} \ , \tag{3}$$

$$(w_{\mathrm{L}})_i = -\frac{k_{ij}}{\mu_{\mathrm{L}}} \left(p_{,j} - \rho_{\mathrm{L}} g_j\right) \ . \tag{4}$$

The mass balance equation describes the hydraulic part including couplings and is given by

$$S_{\mathrm{THM}}\, \dot{p} - \underbrace{\left[\phi_{\mathrm{F}} \beta_T^{\mathrm{L}} + 3(\alpha_{\mathrm{B}} - \phi_{\mathrm{F}}) \alpha_T^{\mathrm{S}}\right]}_{\beta_T^{\mathrm{eff}}} \dot{T} + \alpha_{\mathrm{B}} \dot{u}_{i,i} + (w_{\mathrm{L}})_{i,i} = Q_{\mathrm{H}} \ , \tag{5}$$

where Q_H is the source term for the fluid, β_T^{L} is the volumetric thermal expansion coefficient of the liquid and α_T^{S} is the linear thermal expansion coefficient of the solid. Considering compressible phases, the storage term in THM models is commonly given as (e.g., [60])

$$S_{\mathrm{THM}} = \frac{\phi_{\mathrm{F}}}{K_{\mathrm{FR}}} + \frac{\alpha_{\mathrm{B}} - \phi_{\mathrm{F}}}{K_{\mathrm{SR}}} \ , \tag{6}$$

[1] For clarity, we use index notation based on subscripts along with Einstein's summation convention. Partial differentiation with respect to spatial coordinates uses the comma notation, time rates are denoted by a dot over the variable.

where the suffix THM denotes the dependencies on thermo-hydro-mechanical processes. The mechanical part can be derived from the momentum balance equations and reads

$$\sigma_{ij,j} + \rho^{\mathrm{eff}} g_i = 0 \ , \tag{7}$$

with $\rho^{\mathrm{eff}} = \phi_{\mathrm{F}}\rho_{\mathrm{L}} + (1-\phi_{\mathrm{F}})\rho_{\mathrm{S}}$ and total stress σ_{ij} which is given by

$$\sigma_{ij} = \sigma'_{ij} - \alpha_{\mathrm{B}} p \delta_{ij} \ , \tag{8}$$

where α_{B} is Biot's coefficient and δ_{ij} refers to Kronecker delta and σ'_{ij} is the effective stress tensor given by means of the thermo-elastic relation

$$\sigma'_{ij} = c_{ijkl} \left(\varepsilon_{kl} - \alpha_T^{\mathrm{S}} \Delta T \delta_{kl} \right) \ , \tag{9}$$

where c_{ijkl} and ε_{ij} are the elasticity and strain tensors, respectively. For the isotropic case, the above equation can be rewritten in terms of its Lamé coefficients G and λ

$$\sigma'_{ij} = 2G\varepsilon_{ij} + \lambda\varepsilon_{kk}\delta_{ij} - \left(\lambda + \frac{2G}{3} \right) \alpha_T^{\mathrm{S}} \Delta T \delta_{ij} \ . \tag{10}$$

3. TH model with thermo-mechanical storage coefficients

To obtain an implicit representation of mechanical phenomena in the mass balance of a TH model, we need to make some simplifying assumptions in order to be able to describe the mechanical behavior in terms of coefficients for pressure and temperature time-derivatives such that the displacement rate in Eq. (5) resolves into pressure and temperature rates. In the following, we present two idealized cases based on different constraints for the total stress and the strain. This idealization notwithstanding, real site-scale stress conditions, e.g., in an underground repository, can be quite complicated depending upon its geological genesis. The mechanical response to thermal and hydraulic changes at the local scale is, however, a combination of local conditions independent of the overall far-field stress state as well as the impact of the far-field conditions themselves, usually imposed via boundary conditions. Therefore, it may be described effectively by a combination of free expansion as there is no general preferential direction and constraints due to the confining rock. This behavior is expected to be also dependent on the problem symmetry and it is a-priori not clear which simplified stress assumptions are to be chosen in a given complex setting in order to obtain a good pressure prediction. The assumptions are first combined with linear isotropic thermo-elasticity, and then cased into an orthotropic framework.

3.1. Isotropic thermo-elasticity

3.1.1. THhyd/iso: constant isotropic stress and isotropic thermo-elasticity

In our first derivation, which we call model THhyd/iso, it is assumed that the total hydrostatic stress σ_m, i.e. the sum of all normal stresses, remains constant. This would be the case in a freely expanding specimen. Taking the time-derivative of Eq. (8) and inserting the Lamé parameters, which provide a sufficient description of the mechanical properties of an isotropic material, we obtain

$$\dot{\sigma}_\mathrm{m} = \frac{1}{3}\dot{\sigma}_{ii} := 0 = \frac{1}{3}\dot{\sigma}'_{ii} - \alpha_\mathrm{B}\dot{p} = \underbrace{\left(\lambda + \frac{2G}{3}\right)}_{K_\mathrm{S}}(\dot{u}_{i,i} - 3\alpha_T^\mathrm{S}\dot{T}) - \alpha_\mathrm{B}\dot{p}\ . \tag{11}$$

Thus, we get for the volume strain rate

$$\dot{u}_{i,i} = \frac{\alpha_\mathrm{B}}{K_\mathrm{S}}\dot{p} + 3\alpha_T^\mathrm{S}\dot{T}\ , \tag{12}$$

which we plug into Eq. (5) such that the mass balance simplifies to

$$0 = \left(S_\mathrm{THM} + \frac{\alpha_\mathrm{B}^2}{K_\mathrm{S}}\right)\dot{p} - (\beta_T^\mathrm{eff} - 3\alpha_\mathrm{B}\alpha_T^\mathrm{S})\dot{T} + (w_\mathrm{L})_{i,i}\ . \tag{13}$$

3.1.2. THuni/iso: uniaxial strain and isotropic thermo-elasticity

As the preceding model may not cover all relevant problems of interest, we derive a second model (THuni/iso) in the following paragraph based on uniaxial strain conditions ($\epsilon_{xx} = \epsilon_{yy} = 0$) and constant vertical normal stress σ_{zz}. Unlike for THhyd/iso, we need to take additional thermal stresses into account, originating from the constrained thermal expansion in the transverse directions:

$$\dot{u}_{i,i} := \dot{u}_{z,z}\ , \tag{14}$$

$$\dot{\sigma}_{zz} := 0 = \dot{\sigma}'_{zz} - \alpha_\mathrm{B}\dot{p} = \underbrace{(\lambda + 2G)}_{E_\mathrm{s}^\mathrm{S}}\left(\dot{u}_{i,i} - \alpha_T^\mathrm{S}\dot{T}\right) - 2\alpha_T^\mathrm{S}\lambda\dot{T} - \alpha_\mathrm{B}\dot{p}\ , \tag{15}$$

with the uniaxial aggregate modulus E_s^S. Analogous to THhyd/iso, we obtain a simplified expression for the mass balance:

$$\dot{u}_{z,z} = \frac{\alpha_\mathrm{B}}{E_\mathrm{s}^\mathrm{S}}\dot{p} + \alpha_T^\mathrm{S}\left(1 + 2\frac{\lambda}{E_\mathrm{s}^\mathrm{S}}\right)\dot{T} \ , \tag{16}$$

$$0 = \left(S_\mathrm{THM} + \frac{\alpha_\mathrm{B}^2}{E_\mathrm{s}^\mathrm{S}}\right)\dot{p} - \left[\beta_T^\mathrm{eff} - \alpha_\mathrm{B}\alpha_T^\mathrm{S}\left(1 + 2\frac{\lambda}{E_\mathrm{s}^\mathrm{S}}\right)\right]\dot{T} + (w_\mathrm{L})_{i,i} \ , \tag{17}$$

$$E_\mathrm{s}^\mathrm{S} = \frac{E(1-\nu)}{(1+\nu)(1-2\nu)} \ , \quad \lambda = \frac{E\nu}{(1+\nu)(1-2\nu)} \ , \tag{18}$$

$$0 = \left(S_\mathrm{THM} + \frac{\alpha_\mathrm{B}^2}{E_\mathrm{s}^\mathrm{S}}\right)\dot{p} - \left[\beta_T^\mathrm{eff} - \alpha_\mathrm{B}\alpha_T^\mathrm{S}\frac{1+\nu}{1-\nu}\right]\dot{T} + (w_\mathrm{L})_{i,i} \ . \tag{19}$$

While there is no straightforward generalization for the general anisotropic case, it is possible to generalize the derivations for orthotropic materials in which the material coordinate system is congruent with the surface normals of the applied boundary conditions. This derivation will be presented in the next paragraph.

3.2. Orthotropic thermo-elasticity

The physical properties of bedded sedimentary and stratified rocks often exhibit anisotropy in their hydraulic, mechanical, and thermal behavior due to their genesis. In most cases, those materials can be described as orthotropic or transversely isotropic (c.f. [61]). This is true, e.g., for clay rock [62, 63], one of the host rocks being considered for high-level radioactive waste storage and relevant as a cap rock in many other applications. Therefore, to further extend the practical relevance of the present considerations, a generalization of the above simplifications THhyd/iso and THuni/iso to orthotropic material conditions is desirable. Orthotropic elasticity is best portrayed by the corresponding stiffness (Voigt) matrix $\tilde{C}_{ij}$ showing the elements of the elastic tensor c_{ijkl} in an easily readable format:

$$\tilde{C} = \begin{pmatrix} \frac{1-\nu_{23}\nu_{32}}{E_2E_3D} & \frac{\nu_{21}+\nu_{31}\nu_{23}}{E_2E_3D} & \frac{\nu_{31}+\nu_{21}\nu_{32}}{E_2E_3D} & 0 & 0 & 0 \\ \frac{\nu_{12}+\nu_{13}\nu_{32}}{E_3E_1D} & \frac{1-\nu_{31}\nu_{13}}{E_3E_1D} & \frac{\nu_{32}+\nu_{31}\nu_{12}}{E_3E_1D} & 0 & 0 & 0 \\ \frac{\nu_{13}+\nu_{12}\nu_{23}}{E_1E_2D} & \frac{\nu_{23}+\nu_{13}\nu_{21}}{E_1E_2D} & \frac{1-\nu_{12}\nu_{21}}{E_1E_2D} & 0 & 0 & 0 \\ 0 & 0 & 0 & G_{23} & 0 & 0 \\ 0 & 0 & 0 & 0 & G_{31} & 0 \\ 0 & 0 & 0 & 0 & 0 & G_{12} \end{pmatrix} \tag{20}$$

with $D = (1 - \nu_{12}\nu_{21} - \nu_{23}\nu_{32} - \nu_{31}\nu_{13} - 2\nu_{12}\nu_{23}\nu_{31})/(E_1E_2E_3)$ and the elastic moduli E_i, G_{ij} and the Poisson's ratios ν_{ij}. A set of nine independent quantities fully defines the material in its symmetry coordinate system. This expression is sufficient to derive expressions for the uniaxial strain case, i.e. generalize THuni/iso to THuni/ortho. For the constant isotropic (hydrostatic) stress part, i.e. the generalization THhyd/iso to THhyd/ortho, we need to define a bulk modulus based from $\tilde{C}$ under the given stress condition.

In addition to the stiffness tensor, we consider the thermal expansion to be anisotropic:

$$\varepsilon_{ij}^{\mathrm{th}} = (\alpha_T^{\mathrm{s}})_{ij} \Delta T \ , \tag{21}$$

where for orthotropy we find in material coordinates:

$$(\alpha_T^{\mathrm{s}})_{ij} = \mathrm{diag}[\alpha_{T;x}^{\mathrm{s}}, \alpha_{T;y}^{\mathrm{s}}, \alpha_{T;z}^{\mathrm{s}}] \ . \tag{22}$$

3.2.1. THhyd/ortho: constant isotropic stress and orthotropic thermo-elasticity

To generalize the first model, we substitute the bulk modulus in Eq. (13) with an average expression for orthotropic conditions. For the general anisotropic case, the bulk modulus K is not uniquely defined. However, it is possible to derive an expression for the bulk modulus from the compliance matrix ($\tilde{C}^{-1}$) assuming orthotropic elasticity (e.g., [64]) that is valid under the given stress condition of THhyd/ortho ($\frac{1}{3}\dot{\sigma}_{ii} := 0$):

$$K_{\mathrm{ortho}} = \frac{E_1 E_2 E_3}{E_1 E_2 + E_1 E_3 (1 - 2\nu_{23}) + E_2 E_3 (1 - 2\nu_{12} - 2\nu_{13})} \ . \tag{23}$$

In the literature, this limiting case is often referred to as Reuss bound [65] on the bulk modulus. Thus, Eq. (13) becomes

$$0 = \left(S_{\mathrm{THM}} + \frac{\alpha_{\mathrm{B}}^2}{K_{\mathrm{ortho}}} \right) \dot{p} - \left(\beta_T^{\mathrm{eff}} - \alpha_{\mathrm{B}} \left(\alpha_T^{\mathrm{S}} \right)_{ii} \right) \dot{T} + (w_{\mathrm{L}})_{i,i} \ . \tag{24}$$

It can easily be verified that for isotropy the expression reduces to Eq. (13).

3.2.2. THuni/ortho: uniaxial strain and orthotropic thermo-elasticity

While mechanical orthotropy had no impact on the temperature coefficient of THhyd/ortho, off-diagonal elements of the stiffness matrix need to be considered, when accounting for the thermal stresses as we did in Eq. (15). Substituting the elastic constants in the derivation of THuni/iso

(Eq. (16)–(19)) by the elements of the Voigt matrix yields

$$\alpha_{\mathrm{B}}\dot{p} = \dot{\sigma}_{zz} = \tilde{C}_{33}\left(\dot{\varepsilon}_{zz} - \alpha^{\mathrm{s}}_{T;z}\dot{T}\right) - \dot{T}\left(\alpha^{\mathrm{s}}_{T;x}\tilde{C}_{13} + \alpha^{\mathrm{s}}_{T;y}\tilde{C}_{23}\right) \ , \tag{25}$$

$$\dot{\varepsilon}_{zz} = \frac{\alpha_{\mathrm{B}}}{\tilde{C}_{33}}\dot{p} + \left(\alpha^{\mathrm{s}}_{T;z} + \alpha^{\mathrm{s}}_{T;x}\frac{\tilde{C}_{13}}{\tilde{C}_{33}} + \alpha^{\mathrm{s}}_{T;y}\frac{\tilde{C}_{23}}{\tilde{C}_{33}}\right)\dot{T} \ , \tag{26}$$

$$0 = \left(\beta + \frac{\alpha^2_{\mathrm{B}}}{\tilde{C}_{33}}\right)\dot{p} - \left[\beta^{\mathrm{eff}}_T - \alpha_{\mathrm{B}}\left(\alpha^{\mathrm{s}}_{T;z} + \alpha^{\mathrm{s}}_{T;x}\frac{\tilde{C}_{13}}{\tilde{C}_{33}} + \alpha^{\mathrm{s}}_{T;y}\frac{\tilde{C}_{23}}{\tilde{C}_{33}}\right)\right]\dot{T} + (w_{\mathrm{L}})_{i,i} \ . \tag{27}$$

Thus, plugging in the Young's moduli and Poisson ratios from the Voigt matrix elements (Eq. (20)), we obtain for Eq. (27):

$$\begin{aligned} 0 = &\left(\beta + \frac{\alpha^2_{\mathrm{B}}(1-\nu_{12}\nu_{21}-\nu_{23}\nu_{32}-\nu_{31}\nu_{13}-2\nu_{12}\nu_{23}\nu_{31})}{E_3(1-\nu_{12}\nu_{21})}\right)\dot{p} \\ &- \left[\beta^{\mathrm{eff}}_T - \alpha_{\mathrm{B}}\left(\alpha^{\mathrm{s}}_{T;z} + \alpha^{\mathrm{s}}_{T;x}\frac{\nu_{13}+\nu_{12}\nu_{23}}{1-\nu_{12}\nu_{21}} + \alpha^{\mathrm{s}}_{T;y}\frac{\nu_{23}+\nu_{13}\nu_{21}}{1-\nu_{12}\nu_{21}}\right)\right]\dot{T} + (w_{\mathrm{L}})_{i,i} \ . \end{aligned} \tag{28}$$

As mentioned before, the above-derived expressions for orthotropic materials are only valid if the material coordinate system coincides with the coordinate system in which the uniaxial strain/constant stress assumptions are made, specifically if $\mathbf{e}_3 \equiv \mathbf{e}_z$. Otherwise, additional shear components need to be taken into account, resulting in non-homogeneous stress and pressure fields, which cannot be captured under the given assumptions.

model	**principal assumptions**	**anisotropy**
THhyd/iso	constant hydrostatic (isotropic) stress	thermo-mechanical isotropy
THhyd/ortho	constant hydrostatic (isotropic) stress	thermo-mechanical orthtotropy
THuni/iso	uniaxial strain, constant normal stress	thermo-mechanical isotropy
THuni/ortho	uniaxial strain, constant normal stress	thermo-mechanical orthtotropy

Table 1: Overview over all derived complexity-reduced TH models

4. Computational aspects

All of the test cases were modeled using the multiphysics finite-element open-source software package OpenGeoSys [66, 67] version 6.3 with some alterations. OpenGeoSys was compiled using Intel's MKL library[2]. The system of linear equations was solved with the Pardiso direct solver from the MKL library as long as model sizes remained small. Due to the significant memory usage of direct solvers, large models with around 100 000 elements required an iterative solution

[2]https://software.intel.com/content/www/us/en/develop/tools/math-kernel-library.html

strategy. For this purpose, we used the BiCGSTAB solver of the Eigen library ([68]) with a Jacobi preconditioner. As interpolation functions, a linear basis or mixed-order Taylor-Hood elements were used depending on the case under study. Details are given in Section 6. The linear equation systems were assembled using the monolithic process implementations of the TH implementation or the full THM implementation available in OpenGeoSys [69]. Nonlinearities are resolved within a Newton-Raphson scheme for the THM process, and a Picard scheme for the TH processes, applying absolute tolerance thresholds of 10^{-5} K for temperature increments and 10^{-2} Pa for pressure increments within non-linear iterations.

The run time comparison tests were conducted on an Intel i7-6850K machine with 3.6 GHz running Linux by utilizing the profiling tool perf[3]. Comparisons were run under practical conditions to give the applying user an estimate of the computational time that can be saved rather than focussing on an exact measurement from a computer science perspective.

5. Verification and application modeling

To verify the derived model equations, we first demonstrate exact correspondence under isotropic as well as orthotropic material conditions, where all assumptions made during the model derivation are fully fulfilled by means of setting corresponding boundary conditions. In a second step, we apply both models, THhyd and THuni, to an example problem of a point heat source in an (an-)isotropic saturated porous medium in order to observe the approximation quality of the various formulations under conditions where the underlying assumptions are no longer fulfilled exactly.

5.1. Verification tests

To demonstrate exact correspondence between the various TH formulations and the full THM model under appropriate conditions, we prepared a single hexahedral element test with spatial dimensions of $50\,\mathrm{m} \times 50\,\mathrm{m} \times 50\,\mathrm{m}$ and prescribed temperature on all six boundaries. Over a time of $10\,\mathrm{s}$[4] with a time step of $0.1\,\mathrm{s}$, we increased the temperature linearly from $T_0 = 293.15\,\mathrm{K}$ to $T_1 = 1.5\,T_0$.

[3]https://perf.wiki.kernel.org/index.php/Main_Page

[4]In the absence of spatial gradients and rate-dependent constitutive models, time can be considered a pseudo time in these single-element test cases. Likewise, the dimensions of the hexahedral element are irrelevant and the test can be considered an element or point test.

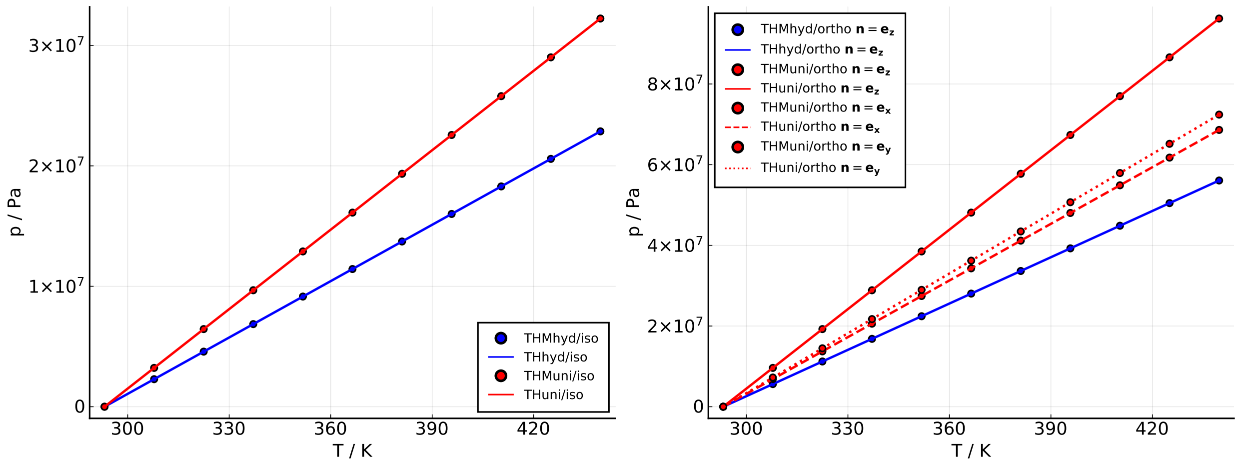

(a) isotropic thermo-elasticity (b) orthotropic thermo-elasticity

Figure 1: Exact correspondence between THM and TH models for given temperature increase and mechanical boundary conditions corresponding to constant hydrostatic stress (iso) or uniaxial strain (uni). Pressure response for isotropic (a) and orthotropic thermo-elasticity with three different orientations (b).

To fulfill the assumptions for THhyd, we require for the corresponding THM model the normal displacement components to vanish for $x = 0$, $y = 0$ and $z = 0$, while we use vanishing normal traction conditions for $x = 50\,\mathrm{m}$, $y = 50\,\mathrm{m}$ and $z = 50\,\mathrm{m}$.

To satisfy the assumptions of the THM model in correspondence with THuni, we imposed vanishing normal displacements at $x = 0$, $y = 0$ and $z = 0$ as well as at $x = 50\,\mathrm{m}$ and $y = 50\,\mathrm{m}$, while we applied vanishing normal traction conditions at $z = 50\,\mathrm{m}$. The set of material parameters is given in Tab A.4.

In Fig. 1a we present the results of the verification test assuming isotropic thermo-elasticity. The pressure response of the TH model agrees (practically speaking) exactly with the corresponding THM counterparts for a given temperature if the TH models are parameterized based on the appropriate assumptions, i.e. THhyd/iso or THuni/iso. This is also true under orthotropic elastic material conditions that were realized by the following set of elastic parameters: $E_1 = 3\,\mathrm{GPa}$, $E_2 = 5\,\mathrm{GPa}$, $E_3 = 7\,\mathrm{GPa}$, $\nu_{12} = 0.23$, $\nu_{23} = 0.33$ and $\nu_{13} = 0.43$. For reasons of simplicity, all thermal expansion coefficients $(\alpha_T^{\mathrm{s}})_{(ii)} = 4.2 \cdot 10^{-6}\,\mathrm{K}^{-1}$ were considered to be equal in all directions; the parentheses indicate suspension of the summation convention. Additionally, the material coordinate system was used in three configurations: (i) as above, as well as rotated by $\frac{\pi}{2}$ around the (ii) y-axis and (iii) x-axis. Due to loading symmetry of the THhyd/ortho models, all three cases trivially agree and only the first case is shown in Fig. 1b. For the THuni/ortho model, which is depicted in Fig. 1b as well, we get three different curves that coincide all very well with their THM counterparts. The THhyd/ortho case produces the lowest thermal pressurization due to an unhindered expansion of the solid matrix and thus the pore space. As confinement increases, thermal pressurization increases by an amount that depends on the anisotropy of the material and its alignment with respect to confinement.

5.2. Application-oriented tests: point heat source

To proceed to more application-oriented examples, we use a model of a point heat source in a fluid-saturated porous medium. This test is inspired by field experiments such as the FE-experiment in Mont Terri (Switzerland) that mimics full-scale the emplacement of a radioactive waste disposal cell in clay host rocks, wherefore we chose to take the material parameters as well as the anisotropy conditions from this underground research laboratory situated in an Opalinus clay formation [70, 71]. The corresponding data are shown in Tab. 2.

For the case of a constant heat source, intrinsically incompressible solid and fluid phases, and spherical symmetry, an analytical solution can be found elsewhere [57, 59] and has been cross-verified with the THM implementation in OpenGeoSys [59]. The model domain consists of a structured mesh with spatial dimensions $10\,\mathrm{m} \times 10\,\mathrm{m} \times 10\,\mathrm{m}$ and 24 389 cells in the isotropic case, and $20\,\mathrm{m} \times 10\,\mathrm{m} \times 20\,\mathrm{m}$ and 97 556 cells in the anisotropic case (Fig. 7a). The greater model domain of the anisotropic model is required due to a lower degree of symmetry resulting for our case in only one symmetry plane. A mesh bias was introduced with a smallest edge length of 0.01 m along each direction at the heat source. As boundary conditions for the displacement components, we use the same configuration as for the model THhyd in the verification test. The anisotropic model mimics a half-space instead of an eighth-space, i.e., Dirichlet boundary conditions were only applied at $y = 0$, while all other boundaries were considered as outer- and thereby free boundaries (free of normal traction). For all outer boundaries, the temperature was required to remain at T_0, whereas, for the pressure, all boundaries were considered to be free (no-flow).

However, it is important to note that the condition of constant hydrostatic total stress is violated at each point within the model domain due to shear stresses induced by incompatible thermal strains due to temperature gradients. That is why we do not expect an exact correspondence between the solutions of the THM and THhyd models.

Table 2: Material parameters for the point heat source model. Numerical indices denote the material coordinate system. Values taken from [70, 71]

Parameter	**symbol**	**value**	**unit**
Young's modulus (isotropic model)	E_{iso}	$8.0 \cdot 10^9$	Pa
Young's moduli (orthotropic model)	$E_1 = E_2$	$8.0 \cdot 10^9$	Pa
	E_3	$4.0 \cdot 10^9$	Pa
Poisson's ratio (isotropic model)	ν_{iso}	0.35	-
Poisson's ratios (orthotropic model)	ν_{12}	0.35	-
	$\nu_{31} = \nu_{32}$	0.25	-
Shear moduli (orthotropic model)	G_{12}	$2.96 \cdot 10^9$	Pa
	$G_{13} = G_{23}$	$1.48 \cdot 10^9$	Pa
Lin. thermal expansion coefficient of the solid	α_T^{S}	$1.7 \cdot 10^{-5}$	K^{-1}
Vol. thermal expansion coefficient of water	β_T^{L}	$3.98 \cdot 10^{-4}$	K^{-1}
Porosity	ϕ_{F}	0.13	-
Water density	ρ_{L}	999.1	$\text{kg}\,\text{m}^{-3}$
Solid grain density	ρ_{S}	2300.0	$\text{kg}\,\text{m}^{-3}$
Specific isobaric heat capacity of water	c_p^{L}	4065.12	$\text{J}\,\text{kg}^{-1}\text{K}^{-1}$
Specific isobaric heat capacity of the solid	c_p^{S}	995.9	$\text{J}\,\text{kg}^{-1}\text{K}^{-1}$
Heat conductivity of water	λ_T^{L}	0.63122	$\text{W}\,\text{m}^{-1}\text{K}^{-1}$
Heat conductivity of the solid (isotropic model)	$\lambda_{T\,\text{iso}}^{\text{s}}$	2.4	$\text{W}\,\text{m}^{-1}\text{K}^{-1}$
Heat conductivity of the solid (orthotropic model)	$\lambda_{T\,11}^{\text{s}} = \lambda_{T\,22}^{\text{s}}$	2.5	$\text{W}\,\text{m}^{-1}\text{K}^{-1}$
	$\lambda_{T\,33}^{\text{s}}$	1.3	$\text{W}\,\text{m}^{-1}\text{K}^{-1}$
Dynamic viscosity of water	μ_{L}	0.0013	Pa s
Intrinsic permeability (isotropic model)	k_{iso}	$5 \cdot 10^{-20}$	m^2
Intrinsic permeability (orthotropic model)	$k_{11} = k_{22}$	$5 \cdot 10^{-20}$	m^2
	k_{33}	$1 \cdot 10^{-20}$	m^2
Power of the heat source	Q	700	W
Initial temperature	T_0	273.15	K
Storage due to phase compressibility	S_{THM}	$3.0 \cdot 10^{-10}$	Pa^{-1}
Biot-Willis coefficient	α_{B}	0.6	-

Isotropic case. In Figs. 2a – 3b, the pore pressure as well as the temperature are given as functions of the radial distance and the time respectively. For the temperature, we see that all four models again yield nearly identical results. This is due to the fact that the temperature change is mainly driven by the power of the heat source and the thermal conductivity, in terms of which both models are indistinguishable, and advection only plays a marginal role due to the low permeability of the clay material. However, the situation is quite different for the hydraulic process. While all curves converge in the far-field, we see that THuni/iso fits significantly better to the fully coupled THM model than THhyd/iso, which appears to be true for all times and radii under scrutiny. At first sight, this result seems to be counter-intuitive, as we applied the same boundary conditions that are assumed to hold for the THhyd model to the model domain. Nevertheless, it becomes more comprehensible if we imagine how the displacement behaves in a spherical coordinate system around the heat source: The expansion elicited by the heat causes only radial displacement, whereas the tangential components are zero everywhere, effectively creating a one-dimensional displacement field. This behavior is at first glance very similar to the principal assumptions of model THuni. In spherical coordinates, however, the two circumferential strains are non-zero and equal u_r/r under such conditions [59]. The consequential volume increase that would drive the model towards the THhyd solution is constrained in the present case due to the confining effect of the surrounding rock mass. Taken together, these considerations explain the better fit of the THuni approximation.

In other words the free boundaries considered in every direction for the THhyd/iso model are not reflected by an expansion acting against the surrounding rock mass. Therefore, THhyd/iso must underestimate the pore pressure. Secondly, from Fig. 2a, it is clear that for small radii, i.e. close to the heat source, the temperature gradient is very high, causing a slight mismatch between model THM and THuni. However, for large radii, the temperature gradient becomes smaller, and the point heat source problem can be very well modeled locally using the simplification of THuni/iso. For comparison, we also plotted the standard TH model without any corrections for the solid's mechanical behavior resulting in a clear overestimation of the pore pressure which is due to the implicit assumption of a rigid solid skeleton.

To get a deeper understanding of the mismatch between the complexity-reduced models and the fully coupled THM model, we evaluated the relative error between the models for different point heat source powers. The relative error is calculated as the deviation of the TH solution from the

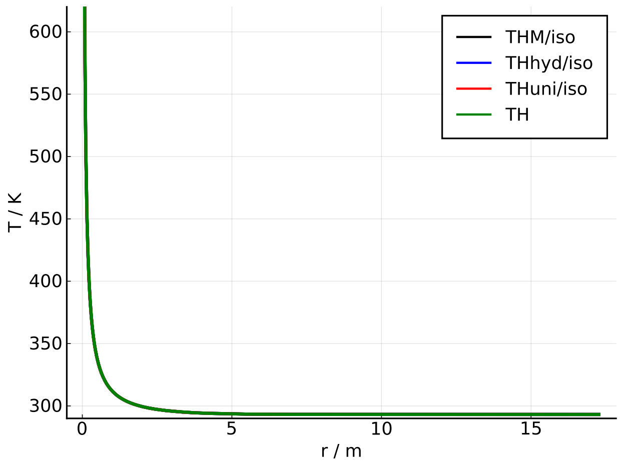

(a) temperature

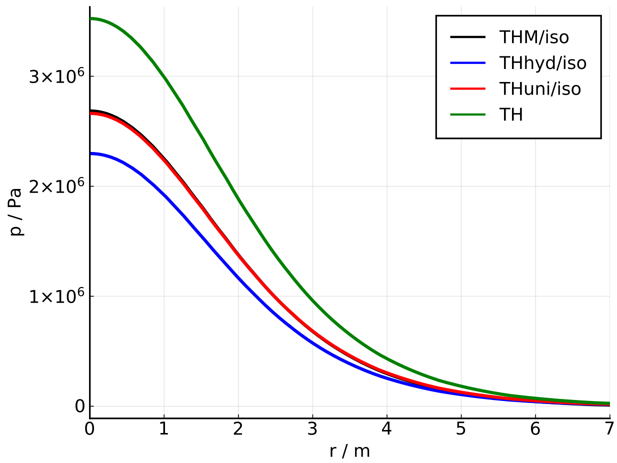

(b) pore pressure

Figure 2: Temperature (a) and pore pressure (b) solution of a coupled THM point heat source problem in an isotropic medium along a diagonal line (1,1,1) extending radially away from the heat source. Solution given at time $t = 5 \cdot 10^6$ s, i.e. about $t = 57.9$ d.

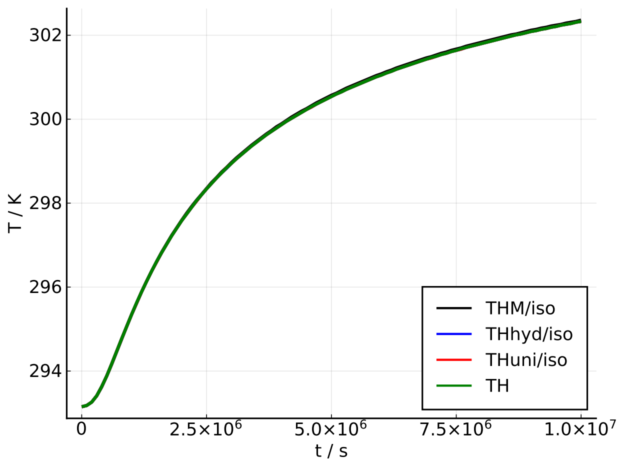

(a) temperature

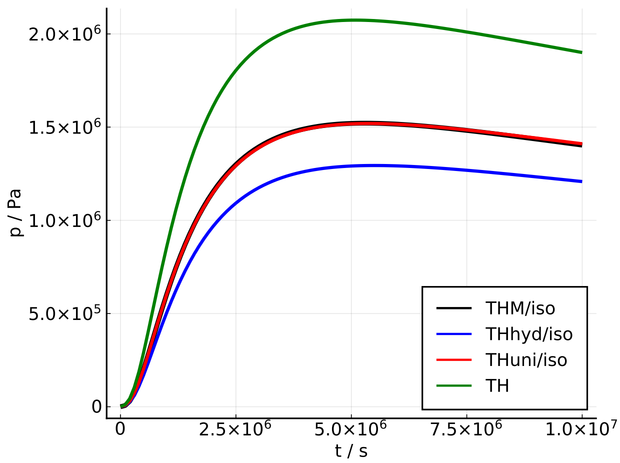

(b) pore pressure

Figure 3: Temperature (a) and pore pressure (b) solution of a coupled THM point heat source problem in an isotropic medium versus time at point P=(1.06,1.06,1.06) m.

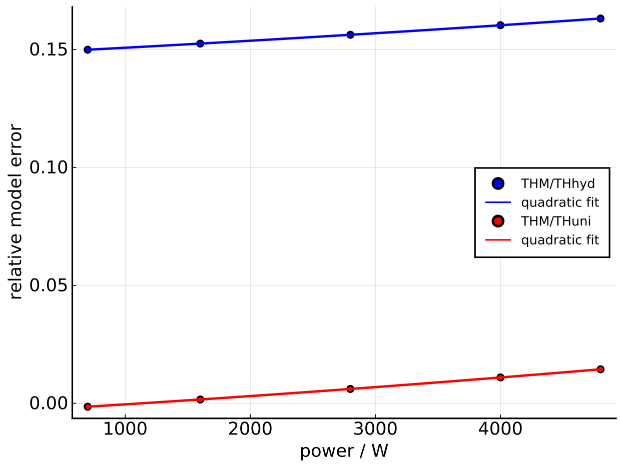

Figure 4: Time averaged model error at point P=(1.06,1.06,1.06) m versus heat source power.

full THM solution. As depicted in Fig. 4, the relative error increases with power in a nearly-linear fashion (fitted using a quadratic function within the applied regime).

Following the argument with the temperature gradient it becomes clear that it explains not only the model mismatch at different locations in space but also the increasing mismatch with increasing power.

Orthotropic case. The shaly facies of the Opalinus clay at the Mt. Terri site is characterized by anisotropic (transversely isotropic) physical properties such as stiffness, strength as well as intrinsic permeability and thermal conductivity. To better represent the geological realities in this application example, anisotropy was incorporated into the model. We assume that the tunnel hosting the heater elements is aligned along the y-direction and that z is the vertical direction. In this coordinate system, the normal of the isotropy plane is given by the anisotropy vector $\mathbf{n} = (-0.573576436, 0.0, 0.819152044)$. For considering anisotropic properties, OpenGeoSys has the ability to define a local coordinate system such that any directional property can be defined in terms of its principal components that are rotated into the global coordinate system accordingly during matrix assembly. While this holds in principle for both types of models (THM and TH), a strategy is needed to consider mechanical anisotropy for our adaptations in the TH models, particularly in the THuni case. While the bulk modulus K_S is invariant under rotations it is a priori not clear how the assigned z-direction of model THuni/ortho should lie with respect to the material coordinate system in our application example.

Therefore, we calculate the thermo-elastic correction terms in model (28) based on the material's transverse isotropic elastic constants, i.e. in the material coordinate system (further denoted as "Re3" for the soft axis and "Re1" for the stiff axes), as well as from the rotated elastic tensor coordinates into direction (1,1,1) (in Figs. 5a – 6b this model is denoted as "R111") in order to achieve an equally weighted average from all directions. The details of this rotation operation and the rotated tensor coordinates can be found in Appendix C.

In Figs. 5a and 6a, we see that as for isotropic material parameters, all temperature predictions agree very well. Deviations can be found again for the pressure solution (Figs. 5b, 6b, 7c, and 7d). Additional to the different alignments of THuni/ortho and THhyd/ortho based on the Reuss bound of the bulk modulus, we added an additional case of THhyd/ortho based on the so called Voigt bound. Instead of hydrostatic stress conditions, the Voigt bound is derived under the assumption of hydrostatic strain and thus, the bulk modulus is deduced from the stiffness matrix instead of the compliance matrix. Therefore, we expect the model to compensate somewhat for the underestimation as it was observered for isotropic material parameters. However, as can be seen in Fig. 5b and 6b, this effect is very small. Analogously, to the isotropic case, we find a strong overestimation in pore pressure for the simple TH model which we attribute to the rigid solid skeleton, keeping in mind that while the anisotropic mechanical response is neglected, the anistropic hydraulic and thermal properties are correctly accounted for. Similar to the isotropic case, we find that the THuni models fit better. As one might expect, the derivation based on the soft axis (Re3) is underestimating the pore pressure, while the derivation of THuni based on the stiff axis (Re1) is overestimating the pore pressure. The best match can found for THuni/ortho R111, which equally weights the mechanical response of all directions. While THuni/ortho R111 contains an effective elastic response without a preferential direction, it might be surprising that it is able to grasp the anisotropic behavior pretty well. However, sensitivity analyses have shown that the evolution of pore pressure is dominated by thermal conductivity and hydraulic permeability [72, 73], which are both fully represented with their anisotropic behavior in all TH models. This happens to be the principal reason why we find a good agreement for anisotropic material parameters as well. This is confirmed by the 3D plots, which show the mirror plane at $y = 0$ to the front (Fig. 7), as well. The temperature profile (Fig. 7b) clearly shows the anisotropy around the heat source origin. Looking at the pressure difference, this region is well described with by model THuni/ortho (Fig. 7d). Nevertheless, we see in both simplified models (Fig. 7c and 7d)

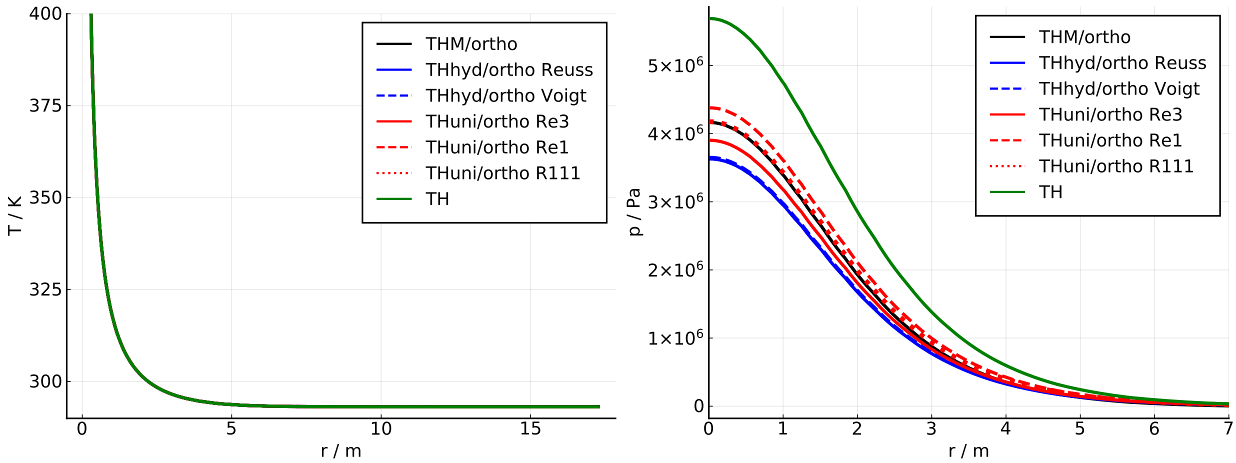

(a) temperature

(b) pore pressure

Figure 5: Temperature (a) and pore pressure (b) solution of a coupled THM point heat source problem in an anisotropic medium along the diagonal (1,1,1) extending radially outward from the heat source at time $t = 5e6$ s.

a small overestimation in pore pressure in the far-field. We attribute this effect to the fact that the directional dependence of the mechanical properties is considered only by averaging over all directions in our simplified models.

5.3. Application-oriented tests: cylindrical heat source in a heterogeneous medium

As a final test case we investigated a more complex case of a cylindrical heat-source surrounded by three different materials: bentonite, a pedestal and the anisotropic clay material. All materials are represented here as linearly elastic, in line with the idea that the presented scheme is used for computationally efficient early scoping calculations. Such analyses should, of course, not replace full THM calculations incorporating the complex THM behaviour of materials such as bentonite or clay rock.

The configuration and the finite-element triangulation is depicted in Fig. 8a. The heater is placed on a compacted bentonite pedestal (red) of thickness 0.8 m and is modeled with a circular boundary with $r = 0.525$ m. The surrounding granular bentonite (white) has a thickness of 0.715 m. The spatial extensions of the model domain are 100 m $\times$ 100 m. The material properties for the clay material were also taken from Tab. 2. The power of the heat source as well as bentonite and pedestal material properties are given in Appendix B. The heat source is represented via Neumann boundary conditions for the energy balance. For the hydraulic process, all boundaries were considered to be no-flow boundaries, whereas the inner boundary as well as the upper and

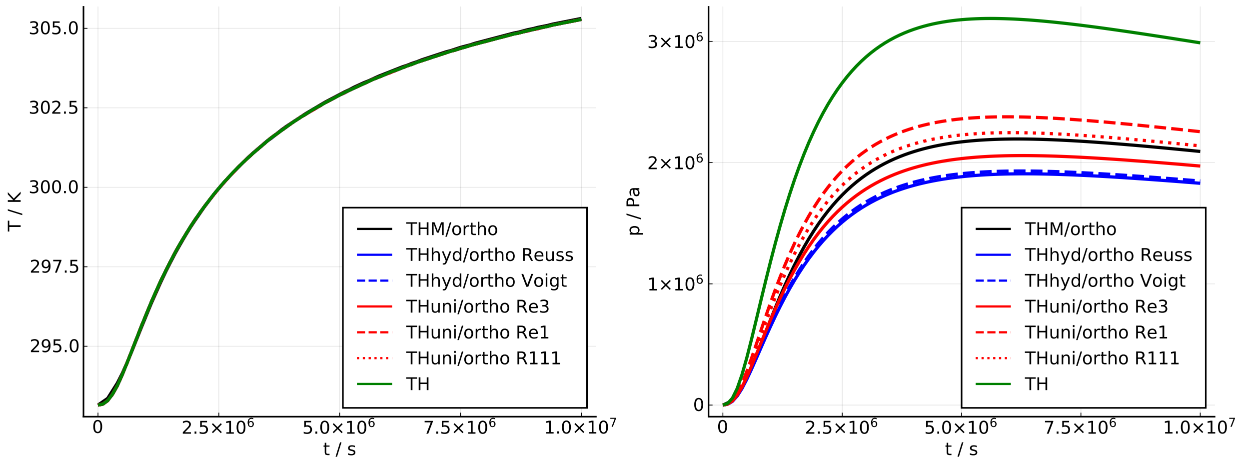

(a) temperature

(b) pore pressure

Figure 6: Temperature (a) and pore pressure (b) solution versus time of a coupled THM point heat source problem in an anisotropic medium at point P=(1.06,1.06,1.06) m.

the right boundary are traction-free boundaries for the mechanical process[5]. For the outer lower and left boundaries, normal displacements were constrained (roller bc). The heater boundary was modelled traction-free as well in this simplified representation.

Whereas the temperature response of all TH models agrees exactly with the full THM model, the behavior of the pressure response requires a closer look. For this purpose, we evaluated the pressure response at three observation points. P1 is placed in the bentonite layer whereas P2 and P3 are placed within the clay material.

For all points, we observe a very strong mismatch between a “rigid” TH model and all other models incorporating mechanical effects. For the near-field point P1 we find that THM, THhyd and THuni behave qualitatively similar, but both complexity-reduced models underestimate the pressure significantly. However, for P2 and P3, which are associated with the intermediate-field region, THuni seems to provide a relatively good prediction, while THiso is underestimating the pore pressure as in the point heat source problem. The underestimation of THuni compared to the fully-coupled THM model for P1 can be explained by the impact of the bentonite–clay interface. The direct material coupling causes an effective stiffening of the bentonite that is pronounced stronger in the THM model. The information about this constraint is propagated through the material via its shear stiffness in the THM model. In contrast, the consideration of mechanical effects in THuni and THhyd is purely local, i.e. neighbouring regions have no effect. From an

[5]Given linearity in the current analysis, the superposition principle holds.

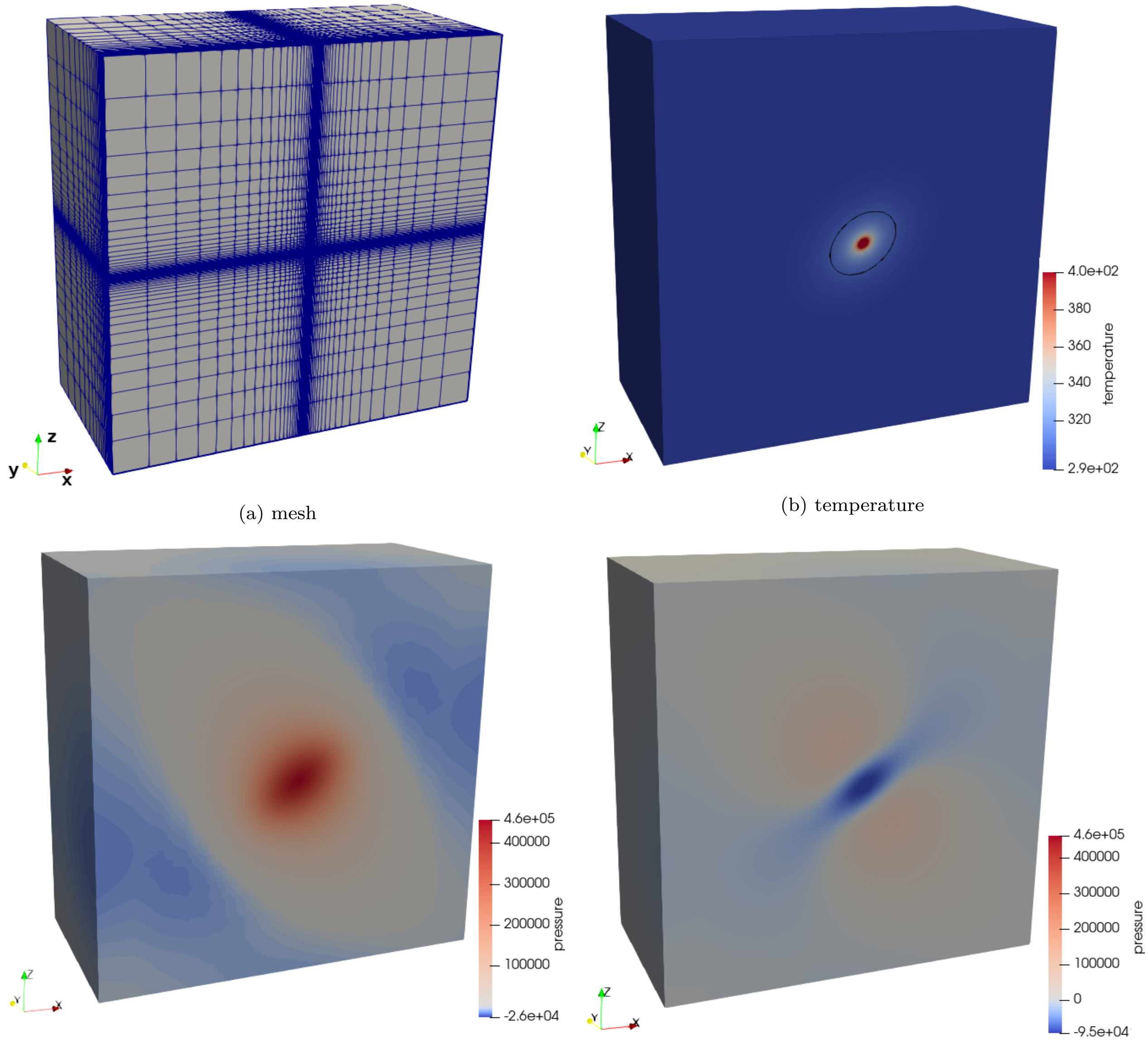

(a) mesh

(b) temperature

(c) $p_{\text{THM}} - p_{\text{THhyd/ortho}}$

(d) $p_{\text{THM}} - p_{\text{THuni/ortho R111}}$

Figure 7: Mesh of orthotropic model (a) and temperature $[T] = \text{K}$, the black ellipse indicates the $T_0 + 10\,\text{K}$ isosurface (b) pore pressure error $[\Delta p] = \text{Pa}$ of THhyd/ortho (c) and pore pressure error $[\Delta p] = \text{Pa}$ of THuni/ortho (d) with respect to the pore pressure of model THM at $t = 5e6\,\text{s}$.

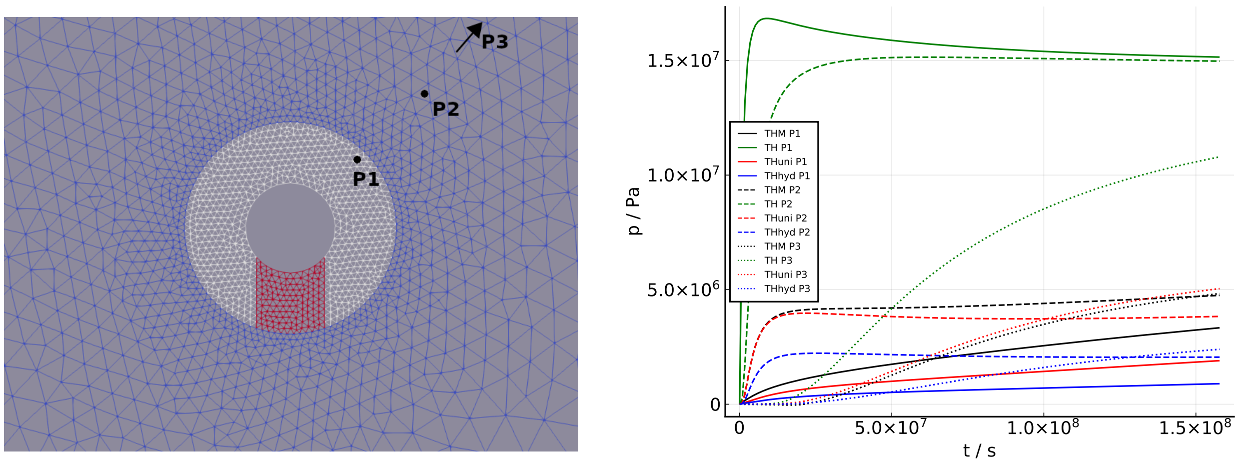

(a) mesh

(b) pore pressure

Figure 8: Mesh of the model domain consisting of three material groups (a) and pore pressure (b) solution versus time of a coupled THM cylindical heat source problem in an anisotropic medium for three points, one within the bentonite domain P1=(0.8,0.8,0.0) m and two points within the clay domain P2=(1.5,1.5,0.0) m. and P3=(10.5,10.5,0.0) m

experimental standpoint, such interfaces behave quite complicated and are usually far from ideal and require careful consideration. Therefore, it is a-priori not clear whether the tight material coupling in the THM model is in all cases a better description of reality. Although, boundaries and interfaces can affect both models differently, we find that THuni is able to give a fairly good estimate for the pore pressure evolution which is a substantial improvement compared to the pristine TH model. A more detailed analyses involving mechanical fields and phenomena such as inelasticity then requires an actual THM analysis.

6. Runtime benchmarks

After showing the applicability of various TH models with consistent thermo-mechanical parameterization, we conducted additional performance tests to get an idea of how much time could be saved compared to running the fully coupled THM model. These tests are based on the point heat source problem, as presented in the previous section. In addition to the meshes used previously, a coarser mesh with a size of 1000 elements (anisotropic: 4000 elements) was used. A rough estimation of how much computing time can be saved based on the idea of linear scaling is done quickly by comparing the number of degrees of freedom, i.e., by multiplying the number of nodes by the number of primary variable components per node. For the full THM model, we have (p, T, u_x ,u_y and u_z), whereas for the TH models, the number of primary variables reduces by a factor of 2/5: p and T. In fact, this constitutes more or less a lower bound as most solvers scale usually worse, dependent very much on the size of the linear system. We also have to add, that as of now, OpenGeoSys uses the Picard solver for the non-linear problem of the TH process, whereas the Newton solver is used for the THM process. The values obtained here can thus not be easily extrapolated to other solvers but do hold some value as practical estimators.

Furthermore, for THM, it is common to use mixed-order Taylor-Hood elements for the primary variables to overcome the problem of pressure oscillations in low-permeable media [74, 75], i.e., while for p and T a linear basis is used, a quadratic approximation space is used for u_i. This, in turn, increases the number of degrees of freedom and thereby the computational cost of the fully coupled THM model even further. For the thus resulting three mesh sizes summarized in Tab. 3, this effect amounts to a factor of roughly 8/3 in terms of degrees of freedom compared to the case where a linear basis is used for all primary variables. Also, full integration on a quadratic mesh implies a higher number of integration points than when using a linear approximation space. For typical Serendipity-class elements in 3D (HEX20 vs. HEX8 for quadratic and linear approximations, respectively), each element would have 27 or 8 integration points, respectively. Note, that this increase in cost comes solely due to the necessity of incorporating deformation processes into the THM models. In other words, both in the THM and the TH models, pore pressure and temperature are merely approximated by linear Ansatz functions and do not benefit from the higher-order elements introduced to stabilize the hydro-mechanical coupling.

The results of the performance tests are presented in Fig. 9 and Tab. 3. Here, for comparability reasons, only data obtained using the Pardiso direct solver is shown (i.e., we skipped the analysis of the normal mesh discretization of the anisotropic model which was solved using the BiCGSTAB solver). While the number of degrees of freedom is decreased by a factor of 5/2, the speed-up is for all meshes nearly about a factor of 10. Likewise, when comparing the case of quadratic elements for the displacement (THM-Q) with the case, where linear elements were used for all variables: While the number of degrees of freedom is reduced by a factor of 3/8, a runtime improvement of about a factor of 4 can be observed for the small mesh up to 10 for the normal mesh. For the normal mesh size, this means a speed-up of about a factor of over 200. Practically speaking, the DoF reduction is most significant when transitioning from a THM model with Taylor-Hood elements to a TH model with linear elements. Note that still, the number of pressure and temperature

Table 3: Models with their corresponding sizes, degrees of freedom (DoF) and their calculated computing (CPU) times. Q indicates the use of Taylor-Hood elements with quadratic approximation of displacement. For all small meshes, we provide the mean and the standard deviation based on 10 repetitions.

Model	(mean) CPU time	DoF
TH small	54.8 ± 0.4	2662
THM small	498.0 ± 8.8	6655
THM small Q	1901.2 ± 4.1	17545
TH aniso small	132.4 ± 0.5	9702
THM aniso small	1456.8 ± 17.4	24255
THM aniso small Q	7547.8 ± 45.0	65205
TH normal	2280	54000
THM normal	48028	135000
THM normal Q	477082	369900

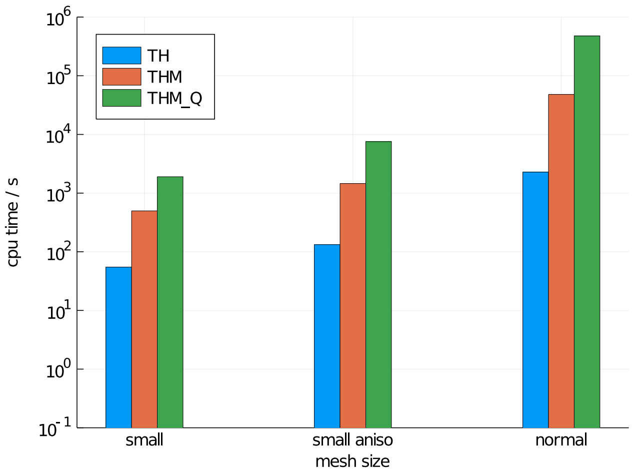

Figure 9: Speed-up between THM and TH models for different mesh sizes.

degrees of freedom remains unchanged during such a transition. Furthermore, as seen in the verification section, the accuracy can be largely maintained when a consistent thermo-mechanical parameterization is chosen for the TH model. To further improve the representation of the far-field in a computationally efficient manner, infinite elements [76] are a viable option as well which may be used in combination with the present approach.

7. Conclusions

Until today, complexity-reduced models are necessary for tasks like framing calculations, sensitivity analyses, parameter identification (by inverse modeling), uncertainty quantification etc. Such simplification for speed-up always has to be balanced with a loss on a case-by-case basis. The present work showed how TH models should be consistently parameterized in order to make quantitative predictions of thermal fluid pressurization comparable to those obtained by fully coupled THM models.

Based on a consistent consideration of thermo-mechanical processes, we derived two model equations that enable the modeling of coupled thermo-hydro-mechanical effects with the computational effort of a hydro-thermal model. The equations hold exactly under well-defined stress and strain conditions in orthotropic porous media but also largely maintain their accuracy in more general cases. The latter was shown for the case of a point and cylindrical heat source in an anisotropic porous medium for which both TH models provided reasonable estimates for pore pressure and temperature despite a violation of the simplifying assumptions made during the derivation of the TH formulations.

Using the finite-element software OpenGeoSys we showed that a speed-up of two orders of magnitude could be reached in some cases. It is important to note that the actual speed-up is strongly dependent on the model size and implementation details. However, the most beneficial results are found for the highest number of degrees of freedom for which complexity-reduction is particularly interesting.

Future studies should investigate similar approximations for unsaturated and inelastic material models and in the presence of heterogeneous mechanical properties.

Acknowledgments

This work was funded in parts by the German Federal Ministry of Education and Research (BMBF) as part of the project Integrity of nuclear waste repository systems – Cross-scale system understanding and analysis – iCross (02NUK053E) and Impulse and Networking Funds of the Helmholtz Association (SO-093). The contribution of SK was funded by the Bundesgesellschaft für Endlagerung (BGE), the German federal company for radioactive waste disposal. DECOVALEX is an international research project comprising participants from industry, government and academia, focusing on development of understanding, models and codes in complex coupled problems in sub-surface geological and engineering applications; DECOVALEX-2023 is the current phase of the project. The authors appreciate and thank the DECOVALEX-2023 Funding Organisations Andra, BASE, BGE, BGR, CAS, CNSC, COVRA, US DOE, ENRESA, ENSI, JAEA, KAERI, NWMO, RWM, SÚRAO, SSM and Taipower for their financial and technical support of the work described

Table A.4: Material parameters for the point heat source model.

Parameter	**symbol**	**value**	**unit**
Young's modulus	E_{iso}	$2.7 \cdot 10^9$	Pa
Poisson's ratio	ν_{iso}	0.33	-
Young's modulus	E_1	$3 \cdot 10^9$	Pa
Young's modulus	E_2	$5 \cdot 10^9$	Pa
Young's modulus	E_3	$7 \cdot 10^9$	Pa
Poisson's ratio	ν_{12}	0.23	-
Poisson's ratio	ν_{23}	0.33	-
Poisson's ratio	ν_{13}	0.43	-
Shear modulus	G_{12}	$1.2 \cdot 10^9$	Pa
Shear modulus	G_{23}	$1.3 \cdot 10^9$	Pa
Shear modulus	G_{13}	$1.4 \cdot 10^9$	Pa
Lin. thermal expansion coefficient of the solid	α_T^{s}	$1.4 \cdot 10^{-6}$	K^{-1}
Vol. thermal expansion coefficient of water	β_T^{L}	$3.98 \cdot 10^{-4}$	K^{-1}
Porosity	ϕ_F	0.183	-
Water density	ρ_{L}	999.1	$\mathrm{kg\,m^{-3}}$
Solid grain density	ρ_{S}	2768.5	$\mathrm{kg\,m^{-3}}$
Specific isobaric heat capacity of water	c_p^{L}	4065.12	$\mathrm{J\,kg^{-1}K^{-1}}$
Specific isobaric heat capacity of the solid	c_p^{S}	860.0	$\mathrm{J\,kg^{-1}K^{-1}}$
Heat conductivity of water	λ_T^{L}	0.63122	$\mathrm{W\,m^{-1}K^{-1}}$
Heat conductivity of the solid	λ_T^{S}	1.7	$\mathrm{W\,m^{-1}K^{-1}}$
Dynamic viscosity of water	μ_{L}	0.001	$\mathrm{Pa\,s}$
Intrinsic permeability	k_{S}	$3 \cdot 10^{-20}$	m^2

in this paper. The statements made in the paper are, however, solely those of the authors and do not necessarily reflect those of the Funding Organisations. We are also very grateful to the OpenGeoSys developer team for their enthusiastic, continuous work on further developing and improving the OGS platform for the scientific community.

Appendix A. Parameters used for showing exact correspondence

Appendix B. Parameters used for cylindrical heat source

Table B.5: Material parameters for bentonite and the pedestal of the cylindrical heat source model. Numerical indices denote the material coordinate system.

Parameter	**symbol**	**value**	**unit**
Young's modulus	E^{bent}	$18.0 \cdot 10^{6}$	Pa
Young's modulus	E^{ped}	$24.0 \cdot 10^{6}$	Pa
Poisson's ratio	ν^{bent}	0.35	-
Poisson's ratio	ν^{ped}	0.2	-
Lin. thermal expansion coefficient	α_T^{bent}	$1.7 \cdot 10^{-5}$	K^{-1}
Lin. thermal expansion coefficient	α_T^{ped}	$3.0 \cdot 10^{-6}$	K^{-1}
Porosity	$\phi_{\mathrm{F}}^{\mathrm{bent}}$	0.331	-
Porosity	$\phi_{\mathrm{F}}^{\mathrm{ped}}$	0.331	-
Solid grain density	$\rho_{\mathrm{S}}^{\mathrm{bent}}$	2232.15	$\mathrm{kg\,m^{-3}}$
Solid grain density	$\rho_{\mathrm{S}}^{\mathrm{ped}}$	2526.16	$\mathrm{kg\,m^{-3}}$
Specific isobaric heat capacity of the solid	c_p^{bent}	800	$\mathrm{J\,kg^{-1}K^{-1}}$
Specific isobaric heat capacity of the solid	c_p^{ped}	800	$\mathrm{J\,kg^{-1}K^{-1}}$
Heat conductivity of the solid	$\lambda_T^{\mathrm{bent}}$	1.79	$\mathrm{W\,m^{-1}K^{-1}}$
Heat conductivity of the solid	$\lambda_T^{\mathrm{bent}}$	1.43	$\mathrm{W\,m^{-1}K^{-1}}$
Intrinsic permeability	k^{bent}	$3.5 \cdot 10^{-20}$	m^2
Intrinsic permeability	k^{ped}	$1.0 \cdot 10^{-22}$	m^2
Power of the heat source	Q	1350	W
Initial temperature	T_0	288.15	K
Biot-Willis coefficient	α_{B}	1.0	-

Appendix C. Stiffness tensor coordinates of Opalinus Clay in global (rotated) coordinate system

In order to perform the coordinate transformation, the stiffness tensor was used in its tensorial form, such that we can write

$$c'_{ijkl} = R_{im}R_{jn}R_{ko}R_{lp}c_{mnop} \ , \tag{C.1}$$

where R_{im} are the components of the rotation matrix, which can be deduced from the anisotropy vector $\mathbf{n} = (n_x, n_y, n_z)^{\mathrm{T}}$ by constructing the following basis:

$$\mathbf{e'}_1 = \left(\frac{n_z}{n_x} \frac{1}{\sqrt{1 + \left(\frac{n_z}{n_x}\right)^2}}, 0, -\frac{1}{\sqrt{1 + \left(\frac{n_z}{n_x}\right)^2}} \right)^{\mathrm{T}} , \tag{C.2}$$

$$\mathbf{e'}_3 = (n_x, n_y, n_z)^{\mathrm{T}} , \tag{C.3}$$

$$\mathbf{e'}_2 = \mathbf{e'}_3 \times \mathbf{e'}_1 . \tag{C.4}$$

This construction is only valid if $n_x \neq 0$, otherwise a separate case needs to be considered:

$$\mathbf{e'}_1 = (1, 0, 0)^{\mathrm{T}} , \tag{C.5}$$

$$\mathbf{e'}_2 = (0, n_z, -n_y,)^{\mathrm{T}} , \tag{C.6}$$

$$\mathbf{e'}_3 = (0, n_y, n_z,)^{\mathrm{T}} . \tag{C.7}$$

If only axes are exchanged, this transformation is trivial. However, we used the (1,1,1) vector in order to obtain an equally weighted average of the elastic properties from all directions. After transforming the elastic tensor back into its Voigt matrix form and inserting the numerical values from Tab. 2, we obtain the rotated stiffness matrix:

$$\tilde{C}' = \begin{pmatrix} 8.84722e9 & 5.97377e9 & 5.92901e9 & 6.32897e7 & 1.31925e9 & -9.32848e8 \\ 5.97377e9 & 1.13945e10 & 6.21502e9 & 1.03956e9 & 5.90952e8 & -1.2732e9 \\ 5.92901e9 & 6.21502e9 & 1.00226e10 & 9.00616e8 & 1.55991e9 & -2.4769e8 \\ 6.32897e7 & 1.03956e9 & 9.00616e8 & 2.41872e9 & -8.73152e7 & 3.64148e8 \\ 1.31925e9 & 5.90952e8 & 1.55991e9 & -8.73152e7 & 2.3179e9 & -6.76556e7 \\ -9.32848e8 & -1.2732e9 & -2.4769e8 & 3.64148e8 & -6.76556e7 & 2.27006e9 \end{pmatrix} \mathrm{Pa} . \tag{C.8}$$

References

[1] F. Parisio, V. Vilarrasa, W. Wang, O. Kolditz, T. Nagel, The risks of long-term re-injection in supercritical geothermal systems, Nature Communications 10 (1) (2019) 1–11.

[2] A. B. Jacquey, M. Cacace, G. Blöcher, N. Watanabe, E. Huenges, M. Scheck-Wenderoth, Thermo-poroelastic numerical modelling for enhanced geothermal system performance: Case study of the Groß Schönebeck reservoir, Tectonophysics 684 (2016) 119–130.

[3] J. Koh, H. Roshan, S. S. Rahman, A numerical study on the long term thermo-poroelastic effects of cold water injection into naturally fractured geothermal reservoirs, Comput. Geotech. 38 (5) (2011) 669–682.

[4] G. Izadi, D. Elsworth, The influence of thermal-hydraulic-mechanical- and chemical effects on the evolution of permeability, seismicity and heat production in geothermal reservoirs, Geothermics 53 (2015) 385–395.
[5] S. De Simone, J. Carrera, V. Vilarrasa, Superposition approach to understand triggering mechanisms of post-injection induced seismicity, Geothermics 70 (2017) 85–97.
[6] B. L. Avanthi Isaka, P. G. Ranjith, Investigation of temperature- and pressure-dependent flow characteristics of supercritical carbon dioxide- induced fractures in Harcourt granite: Application to CO2-based enhanced geothermal systems, Int. J. Heat Mass Transf. 158 (2020) 119931.
[7] A. Ranjbar, H. Hassani, K. Shahriar, M. J. A. Shahrabi, Thermo-hydro-mechanical modeling of fault discontinuities using zero-thickness interface element, J. Rock Mech. Geotech. Eng. 12 (1) (2020) 74–88.
[8] H. Rattez, I. Stefanou, J. Sulem, The importance of Thermo-Hydro-Mechanical couplings and microstructure to strain localization in 3D continua with application to seismic faults. Part I: Theory and linear stability analysis, J. Mech. Phys. Solids 115 (2018) 54–76.
[9] Q. Zeng, J. Yao, J. Shao, An extended finite element solution for hydraulic fracturing with thermo-hydro-elastic–plastic coupling, Comput. Methods Appl. Mech. Eng. 364 (2020) 112967.
[10] N. Noii, T. Wick, A phase-field description for pressurized and non-isothermal propagating fractures, Comput. Methods Appl. Mech. Eng. 351 (2019) 860–890.
[11] R. Gelet, B. Loret, N. Khalili, A thermo-hydro-mechanical coupled model in local thermal non-equilibrium for fractured HDR reservoir with double porosity, J. Geophys. Res. Solid Earth 117 (B7) (2012).
[12] T. Teng, Y. Zhao, F. Gao, J. G. Wang, W. Wang, A fully coupled thermo-hydro-mechanical model for heat and gas transfer in thermal stimulation enhanced coal seam gas recovery, Int. J. Heat Mass Transf. 125 (2018) 866–875.
[13] B. Loret, Carbon Dioxide Sequestration and Enhanced Recovery Techniques, Springer, 2019, pp. 681–750.
[14] P.-Z. Pan, J. Rutqvist, X.-T. Feng, F. Yan, Modeling of caprock discontinuous fracturing during CO2 injection into a deep brine aquifer, International Journal of Greenhouse Gas Control 19 (2013) 559–575.
[15] J. Rutqvist, Status of the TOUGH-FLAC simulator and recent applications related to coupled fluid flow and crustal deformations, Comput. Geosci. 37 (6) (2011) 739–750.
[16] B. Bary, G. Ranc, S. Durand, O. Carpentier, A coupled thermo-hydro-mechanical-damage model for concrete subjected to moderate temperatures, Int. J. Heat Mass Transf. 51 (11) (2008) 2847–2862.
[17] S. Na, W. Sun, Computational thermo-hydro-mechanics for multiphase freezing and thawing porous media in the finite deformation range, Comput. Methods Appl. Mech. Eng. 318 (2017) 667–700.
[18] D. Salciarini, F. Ronchi, C. Tamagnini, Thermo-hydro-mechanical response of a large piled raft equipped with energy piles: a parametric study, Acta Geotechnica 12 (4) (2017) 703–728.
[19] K. Wang, X. Song, Strain localization in non-isothermal unsaturated porous media considering material heterogeneity with stabilized mixed finite elements, Comput. Methods Appl. Mech. Eng. 359 (2020) 112770.
[20] S. Uchida, K. Soga, A. Klar, K. Yamamoto, Geomechanical study of the Mallik gas hydrate production field trials, Bull. Geol. Surv. Can. 601 (2012) 191–204.
[21] Y. Wang, T. Li, Y. Chen, G. Ma, A three-dimensional thermo-hydro-mechanical coupled model for enhanced geothermal systems (EGS) embedded with discrete fracture networks, Comput. Methods Appl. Mech. Eng. 356 (2019) 465–489.
[22] M. Najari, A. Selvadurai, Thermo-hydro-mechanical response of granite to temperature changes, Environ. Earth Sci. 72 (1) (2014) 189–198.
[23] D. F. Ruiz Restrepo, Thermo-Mechanical analysis of the stability of a rock-cliff under climatic actions, Master's thesis, Universitat Politècnica de Catalunya (2013).
[24] W. Rühaak, L. Pei, J. Bartels, C.-D. Heldmann, S. Homuth, I. Sass, Thermo-hydro-mechanical-chemical coupled modeling of geothermal doublet systems in limestones, 2015, pp. 19–25.
[25] W. Wang, R. Regueiro, M. Stewart, J. McCartney, Coupled thermo-poro-mechanical finite element analysis of an energy foundation centrifuge experiment in saturated silt, 2012, pp. 4406–4415.
[26] J. Tremosa, H. Gailhanou, C. Chiaberge, R. Castilla, E. C. Gaucher, A. Lassin, C. Gout, C. Fialips, F. Claret, Effects of smectite dehydration and illitisation on overpressures in sedimentary basins: A coupled chemical and thermo-hydro-mechanical modelling approach, Mar. Pet. Geol. 111 (2020) 166–178.
[27] A. K. Schneider, Assessing Stability of Coastal Bluffs Due to Combined Actions of Waves and Changing Ambient Temperatures in the Arctic, Master's thesis, Norwegian University of Science and Technology (2017).
[28] J. Hubert, X. Liu, F. Collin, Numerical modeling of the long term behavior of Municipal Solid Waste in a bioreactor landfill, Comput. Geotech. 72 (2016) 152–170.
[29] F. Collin, J. Hubert, X. Liu, B. Cerfontaine, Numerical modelling of a Municipal Waste Disposal as a Bio-Chemo-Thermo-Hydro-Mechanical problem, Coupled and multiphysics phenomena (2015) 259–281.

[30] D. Xiao, W. Xu, L. Zhan, Y. Chen, A Model for Aerobic Biochemical Degradation of Municipal Solid Waste, 2019, pp. 263–271.
[31] K. Li, W. Xu, Y. Chen, A new consolidation model for unsaturated high-kitchen-waste-content msw, Environ. Sci. Eng. (2019) 68–76Cited By 0.
[32] M. M. Tamizdoust, O. Ghasemi-Fare, A fully coupled thermo-poro-mechanical finite element analysis to predict the thermal pressurization and thermally induced pore fluid flow in soil media, Comput. Geotech. 117 (2020) 103250.
[33] H. Xu, J. Rutqvist, C. Plúa, G. Armand, J. Birkholzer, Modeling of thermal pressurization in tight claystone using sequential THM coupling: Benchmarking and validation against in-situ heating experiments in COx claystone, Tunn. Undergr. Space Technol. 103 (2020) 103428.
[34] T. S. Nguyen, Thermo-Hydro-Mechanical-Chemical processes in geological disposal of radioactive waste–An example of regulatory research, Advances in Geo-Energy Research 2 (2) (2018) 173–189.
[35] M. Jobmann, A. Bebiolka, V. Burlaka, P. Herold, S. Jahn, A. Lommerzheim, J. Maßmann, A. Meleshyn, S. Mrugalla, K. Reinhold, A. Rübel, L. Stark, G. Ziefle, Safety assessment methodology for a German high-level waste repository in clay formations, J. Rock Mech. Geotech. Eng. 9 (5) (2017) 856–876.
[36] Y. Chen, S. Zhou, R. Hu, C. Zhou, Estimating effective thermal conductivity of unsaturated bentonites with consideration of coupled thermo-hydro-mechanical effects, Int. J. Heat Mass Transf. 72 (2014) 656–667.
[37] X. Liu, G. Cai, L. Liu, S. Liu, A. J. Puppala, Thermo-hydro-mechanical properties of bentonite-sand-graphite-polypropylene fiber mixtures as buffer materials for a high-level radioactive waste repository, Int. J. Heat Mass Transf. 141 (2019) 981–994.
[38] A. Schäfers, A. Gens, A. Rodriguez-Dono, S. Baxter, V. Tsitsopoulos, D. Holton, D. Malmberg, M. Sawada, Q. Yafei, A. Ferrari, L. Laloui, A. Sjöland, Increasing understanding and confidence in thm simulations of engineered barrier systems, Environ. Geotech. 7 (1) (2020) 59–71.
[39] B. Garitte, H. Shao, X. Wang, T. Nguyen, Z. Li, J. Rutqvist, J. Birkholzer, W. Wang, O. Kolditz, P. Pan, et al., Evaluation of the predictive capability of coupled thermo-hydro-mechanical models for a heated bentonite/clay system (HE-E) in the Mont Terri Rock Laboratory, Environ. Earth Sci. 76 (2) (2017) 64.
[40] J. Rutqvist, C.-F. Tsang, Multiphysics processes in partially saturated fractured rock: Experiments and models from Yucca Mountain, Rev. of Geophys. 50 (3) (2012).
[41] W. Sun, An integrated multiscale experimental-numerical analysis on reconsolidation of salt-clay mixture for disposal of heat-generating waste, Tech. rep., The Trustees of Columbia University in the City of New York (2019).
[42] M. Najari, A computational and experimental modelling of thermo-hydro-mechanical processes in a low permeability granite, Ph.D. thesis, McGill University (2014).
[43] M. Lesueur, T. Poulet, M. Veveakis, Three-scale multiphysics finite element framework (FE3) modelling fault reactivation, Comput. Methods Appl. Mech. Eng. 365 (2020) 112988.
[44] D. Green, H. Wang, Specific storage as a poroelastic coefficient, Water Resour. Res. 26 (7) (1990) 1631–1637.
[45] H. Wang, Theory of Linear Poroelasticity with Applications to Geomechanics and Hydrogeology, Princeton Series in Geophysics, Princeton University Press, 2000.
[46] K. E. Thatcher, A. E. Bond, S. Norris, Pore pressure response to disposal of heat generating radioactive waste in a low permeability host rock, Int. J. Rock Mech. Min. Sci. 135 (2020) 104456.
[47] P. Chen, M. Meng, S. Miska, M. Yu, E. Ozbayoglu, N. Takach, Study on integrated effect of PDC double cutters, Journal of Petroleum Science and Engineering 178 (2019) 1128–1142.
[48] L. C. Murdoch, L. N. Germanovich, Storage change in a flat-lying fracture during well tests, Water Resources Research 48 (12) (2012).
[49] S. A. Mathias, S. Nielsen, R. L. Ward, Storage Coefficients and Permeability Functions for Coal-Bed Methane Production Under Uniaxial Strain Conditions, Transport in Porous Media 130 (2) (2019) 627–636.
[50] W. Rühaak, V. F. Bense, I. Sass, 3D hydro-mechanically coupled groundwater flow modelling of Pleistocene glaciation effects, Comput. Geosci. 67 (2014) 89–99.
[51] B. Garitte, T. Nguyen, J. Barnichon, B. Graupner, C. Lee, K. Maekawa, C. Manepally, G. Ofoegbu, B. Dasgupta, R. Fedors, et al., Modelling the Mont Terri HE-D experiment for the Thermal–Hydraulic–Mechanical response of a bedded argillaceous formation to heating, Environ. Earth Sci. 76 (9) (2017) 345.
[52] F. Magri, J. Maßmann, W. Wang, K. Benisch, Coupled THM processes, Springer, 2015, pp. 221–245.
[53] W. Wang, H. Shao, T. Nagel, O. Kolditz, Analysis of coupled thermal-hydro-mechanical processes during small scale in situ heater experiment in Callovo-Oxfordian clay rock introducing a failure-index permeability model, Int. J. Rock Mech. Min. Sci. (2020) –.
[54] R. Lewis, B. Schrefler, The Finite Element Method in the Static and Dynamic Deformation and Consolidation

of Porous Media, 1st Edition, J. Wiley and Sons, 1998.

[55] W. Ehlers, J. Bluhm, Porous Media: Theory, Experiments and Numerical Applications, 1st Edition, Springer, 2002.

[56] J. R. Booker, C. Savvidou, Consolidation around a spherical heat source, Int. J. Solids Struct. (1984).

[57] J. R. Booker, C. Savvidou, Consolidation around a point heat source., Int. J. Numer. Anal. Methods. Geomech. 9 (2) (1984) 173–184.

[58] D. F. McTigue, Thermoelastic response of fluid-saturated porous rock, J. Geophys. Res. (1986).

[59] A. A. Chaudhry, J. Buchwald, O. Kolditz, T. Nagel, Consolidation around a point heat source (correction and verification), Int. J. Numer. Anal. Methods. Geomech. 43 (18) (2019) 2743–2751.

[60] B. Garitte, T. Nguyen, J. Barnichon, B. Graupner, C. Lee, K. Maekawa, C. Manepally, G. Ofoegbu, B. Dasgupta, R. Fedors, et al., Modelling the mont terri he-d experiment for the thermal–hydraulic–mechanical response of a bedded argillaceous formation to heating, Environ. Earth Sci. 76 (9) (2017) 345.

[61] B. Amadei, Importance of anisotropy when estimating and measuring in situ stresses in rock, Int. J. Rock Mech. Min. Sci. Geomech. 33 (3) (1996) 293–325.

[62] S. Salager, B. François, M. Nuth, L. Laloui, Constitutive analysis of the mechanical anisotropy of opalinus clay, Acta Geotech. 8 (2) (2013) 137–154.

[63] L.-M. Guayacán-Carrillo, S. Ghabezloo, J. Sulem, D. M. Seyedi, G. Armand, Effect of anisotropy and hydro-mechanical couplings on pore pressure evolution during tunnel excavation in low-permeability ground, Int. J. Rock Mech. Min. Sci. 97 (February) (2017) 1–14.

[64] V. Bucur, Bulk and surface waves for wood anisotropy characterization, Materials Science and Engineering A (1989).

[65] J. P. Watt, Hashin-Shtrikman bounds on the effective elastic moduli of polycrystals with orthorhombic symmetry, J. Appl. Phys. 50 (10) (1979) 6290–6295.

[66] O. Kolditz, S. Bauer, L. Bilke, N. Böttcher, J. O. Delfs, T. Fischer, U. J. Görke, T. Kalbacher, G. Kosakowski, C. I. McDermott, C. H. Park, F. Radu, K. Rink, H. Shao, H. B. Shao, F. Sun, Y. Y. Sun, A. K. Singh, J. Taron, M. Walther, W. Wang, N. Watanabe, Y. Wu, M. Xie, W. Xu, B. Zehner, OpenGeoSys: An open-source initiative for numerical simulation of thermo-hydro-mechanical/chemical (THM/C) processes in porous media, Environ. Earth Sci. 67 (2) (2012) 589–599.

[67] L. Bilke, B. Flemisch, T. Kalbacher, O. Kolditz, R. Helmig, T. Nagel, Development of open-source porous-media simulators: principles and experiences., Transp. Porous. Media. (2019).

[68] G. Guennebaud, B. Jacob, et al., Eigen v3, http://eigen.tuxfamily.org (2010).

[69] O. Kolditz, T. Nagel, H. Shao, W. Wang, S. Bauer (Eds.), Thermo-Hydro-Mechanical-Chemical Processes in Fractured Porous Media: Modelling and Benchmarking, Terrestrial Environmental Sciences, Springer International Publishing, Cham, 2018.

[70] H. R. Müller, B. Garitte, T. Vogt, S. Köhler, T. Sakaki, H. Weber, T. Spillmann, M. Hertrich, J. K. Becker, N. Giroud, V. Cloet, N. Diomidis, T. Vietor, Implementation of the full-scale emplacement (FE) experiment at the Mont Terri rock laboratory, in: Swiss J. Geosci., Vol. 110, Springer, 2017, pp. 287–306.

[71] M. Bossart, P. Thurry, Characteristics of the Opalinus Clay at Mont Terri, Reports of the Swiss Geological Survey no. 3 (3) (2008) 26.

[72] B. et al., Doe-based history matching for probabilistic uncertainty quantification of thermo-hydro-mechanical processes around heat sources in clay rocks, -Submitted (2020).

[73] C. et al., Local and global spatio-temporal sensitivity analysis of thermal consolidation around a point heat source, -Submitted (2020).

[74] M. Rahrah, L. A. Lopez-Peña, F. Vermolen, B. Meulenbroek, Network-inspired versus Kozeny-Carman based permeability-porosity relations applied to Biot's poroelasticity model, J. Math. Ind. 10 (1) (2020) 1–21. `arXiv:2004.09373`.

[75] J. B. Haga, H. Osnes, H. P. Langtangen, On the causes of pressure oscillations in low-permeable and low-compressible porous media, Int. J. Numer. Anal. Methods. Geomech. 36 (12) (2012) 1507–1522.

[76] B. Schrefler, L. Simoni, Non-isothermal consolidation of unbounded porous media using mapped infinite elements, Commun. Appl. Numer. Methods 3 (5) (1987) 445–452.